



Atomically integration of O-bridged Co-Fe hetero-pairs as tandem photocatalyst towards highly efficient hydroxyl radicals production

Yali Luo^a, Yang Deng^{a,*}, Pengfei Li^b, Ruoyun Gao^a, Ruijuan Bian^a, Xu Wu^{a,b,*}

^a College of Chemistry, Taiyuan University of Technology, Taiyuan, Shanxi 030024, China

^b College of Chemical Engineering and Technology, Taiyuan University of Technology, Taiyuan, Shanxi 030024, China

ARTICLE INFO

Keywords:

Hetero-atom pairs
Covalent organic framework
Tandem photocatalyst
Hydroxyl radical formation
Wastewater treatment

ABSTRACT

Photocatalytic Fenton-coupled oxygen reduction reaction (ORR) is a promising strategy generated by •OH. Single-atom catalysts (SACs), featuring high atom utilization, exhibit superior catalytic activity. However, effectively catalyzing the two steps on the activity site remains a challenge. Herein, a novel Co-Fe hetero-atom pair tandem photocatalyst was precisely constructed by pre-designing the structure of covalent organic frameworks (COFs) and the introduction strategies of active sites. Thanks to the synergism of adjacent Co-Fe atoms, Co-Fe-COF presents highly efficient hydroxyl radicals production following the process of $O_2 + H_2O \rightarrow H_2O_2 \rightarrow \bullet OH$. Additionally, immobilization of atom pairs on the pore walls of COF can boost the enrichment for contaminants, thus increasing the •OH utilization rates. Theoretical simulations reveal proximity electronic effect of O-bridged Co-Fe not only thermodynamically promotes the formation of OOH^* , but also dynamically activates the self-healing cycle of Fe(II)/Fe(III). This work provides a novel program for designing high-performance tandem catalysts.

1. Introduction

Fenton reaction is an advanced oxidation technology that efficiently removes refractory organic pollutants, which relies on the strongly reducing Fe^{2+} to decompose H_2O_2 to produce highly oxidizing hydroxyl radicals (•OH)[1–3]. However, the continuous generation of •OH in Fenton reaction is largely limited by the slow regeneration of Fe^{2+} , which requires constant input of a large amount of iron slurry, and the inability to generate H_2O_2 itself, which not only causes certain pollution to the environment but also increases the operating cost[4–7]. The heterogeneous Fenton reaction coupled photocatalytic oxygen reduction reaction (ORR) can generate H_2O_2 through the sequential reaction of double electron ORR, and then further activated to generate •OH, thus avoiding additional H_2O_2 addition in Fenton reaction. However, efficiently catalyzing both selective H_2O_2 generation and live H_2O_2 generation •OH tandem generation on a single catalyst remains a major challenge[8–11].

Single-atom catalysts (SACs), with the maximized atomic utilization and tunable electronic properties, exhibit significant advantages in catalysis, particularly in the field of energy storage and conversion[12, 13]. However, SACs also possess notable limitations in multifunctional

catalysis, presenting great challenges to their application. Diatomic catalysts (DACs) have emerged as a potential solution to address the catalytic shortcomings associated with traditional SACs[14]. DACs provide dual active sites that can independently bind different intermediates and catalyze the continuous reaction steps, greatly improving the activity and selectivity of multiple-step catalytic reactions[15,16]. DACs can ensure a high loading of metal atoms while maintaining overall photocatalyst activity, representing a significant advancement in this field of development. In addition, DACs also precisely regulates electron density through electron orbital interactions at atomic positions, creating favorable conditions for the rapid transfer and separation of photoinduced electron-hole pairs and the capture of visible light, thereby optimizing the adsorption energy of reaction intermediates, thereby enhancing the inherent activity of the photocatalyst[17,18]. Therefore, developing novel hetero-atom pair tandem catalyst is a promising strategy for the high-efficiency generation of H_2O_2 and activation of H_2O_2 to •OH[19,20].

Covalent organic frameworks (COFs) is a class of organic porous crystalline polymers with light elements (C, O, N, B, etc.) connected by covalent bonds, which can accurately construct organic unit atoms into periodic frames with extended structures with ordered nanopore

* Corresponding authors at: College of Chemistry, Taiyuan University of Technology, Taiyuan, Shanxi 030024, China.

E-mail addresses: dengyang@tyut.edu.cn (Y. Deng), wuxu@tyut.edu.cn (X. Wu).

<https://doi.org/10.1016/j.apcatb.2024.124255>

Received 15 April 2024; Received in revised form 15 May 2024; Accepted 30 May 2024

Available online 31 May 2024

0926-3373/© 2024 Elsevier B.V. All rights are reserved, including those for text and data mining, AI training, and similar technologies.

[21–23]. The excellent properties of good crystallinity, low density, high specific surface area and strong structural designability make COFs an emerging material platform for structural control and functional design [24]. In fact, the unique properties and functions of the COFs structure stem from the fact that it provides a new molecular platform for the interaction of photons, excitons, electrons, holes, ions, and guest molecules [25,26].

Herein, we developed a unique O-bridged hetero-atom pair Co-Fe tandem photocatalyst based on pre-design reticular supramolecular COF for high-efficiency catalysis of $\text{O}_2 + \text{H}_2\text{O} \rightarrow \text{H}_2\text{O}_2 \rightarrow \bullet\text{OH}$ [27]. The detailed conformational and coordination structures of the heteroatom pair Co-Fe were revealed by spherical aberration corrected scanning transmission electron microscopy and extended X-ray absorption fine structure. The findings demonstrate that the atomically dispersed Co site exhibits selective H_2O_2 generation, while the Fe site promotes $\bullet\text{OH}$ production through activation of generated H_2O_2 [28]. Both experimental and theoretical simulations confirm the modulation of binding energy for $\bullet\text{OOH}$ at the Co site and $\bullet\text{H}_2\text{O}_2$ at the Fe site. Furthermore, unique O-bridging isomeric atom pairs facilitate electron transfer from Co to Fe, enabling self-healing of Fe(II) [29]. The prepared Co-Fe-COF photocatalyst shows excellent degradation efficiency towards various organic pollutants. This study offers a valuable approach for designing efficient tandem catalysts [26,30].

2. Experimental section

2.1. Instrument

The morphology and elemental mapping of the nanoclusters were characterized by transmission electron microscopy (TEM, JEOL JEM-F200, Japan) and scanning electron microscopy (SEM, JSM-7900 F, Japan). High-resolution transmission electron microscope (HRTEM) measurements were performed on a JEM-3010. X-ray diffraction (XRD) was conducted using a DX-2700B with Cu-K α radiation ($\lambda = 0.15406$ nm). X-ray photoelectron spectroscopy (XPS) measurements were conducted using a Thermo Scientific ESCALAB 250Xi instrument. Fourier transform infrared spectrometer (FT-IR) was tested by Bruker TENSOR II. The Bruker TENSOR II, which had a PIKE DRIFT reaction cell and a mercury-cadmium-telluride (MCT) detector, used in situ DRIFTS. The UV–vis diffuse reflectance spectra (UV–vis DRS) measurements of all samples were performed using a Lambda 850+ (PerkinElmer) spectrophotometer with an integrating sphere equipment. Time-resolved fluorescence decay spectra and Steady-state photoluminescence (PL) spectra were acquired with a FLS980 fluorescence spectrometer. The electron paramagnetic resonance (EPR, Bruker EMX plus) tests were employed to monitor the $\bullet\text{OH}$ generated. X-ray absorption spectra (XAS) including X-ray absorption near-edge structure (XANES) and extended X-ray absorption fine structure (EXAFS) of the samples were collected at the instrumental analysis center of Taiyuan University of Technology. Density functional theory (DFT) calculations were performed using the Dmol3 module of Material Studio 2020.

2.2. Chemicals

All solvents and materials in this study were purchased from commercial sources without further purification. 2,4,6-tri(4-aminophenyl)-1,3,5-triazine (TTA), 2,2-bipyridine-5,5-dialdehyde, tri-fluoromethanesulfonic acid, norfloxacin and bisphenol A were purchased from HEOWNS Biochemical Technology (Tianjin, China). Potassium biphthalate were obtained from MACKLIN Biochemical Technology (Shanghai, China). Cobalt (II) acetate, tetrahydrate ($\text{C}_4\text{H}_6\text{CoO}_4 \cdot 4 \text{H}_2\text{O}$), Ferrous (II) chloride tetrahydrate ($\text{FeCl}_2 \cdot 4 \text{H}_2\text{O}$), Mesitylene, 1,4-dioxane, Potassium chloride (KCl), N, N-Dimethylformamide (DMF) and Tetracycline (TC) were provided by Aladdin (Shanghai, China).

2.3. Materials and synthetic procedures

2.3.1. Synthesis of TTA-BPY-COF

The Pyrex tube filled with 2,4,6-tri(4-aminophenyl)-1,3,5-triazine (18 mg, 0.05 mmol), 2,2-bipyridine-5,5-dialdehyde (11 mg, 0.05 mmol), 1 mL dioxane/mesitylene (V/V=1:1) and 20 μL tri-fluoromethanesulfonic acid was dispersed by ultrasonic for 20 min, and then three freezer-pump-thawing cycles degassing was performed. The above system was put in the oven and heat at 120 $^\circ\text{C}$ for 72 h. After the reaction, the suspended solids were collected by centrifugation and thoroughly cleaned with ethanol (3×15 mL) and acetone (3×15 mL) respectively. The production was dried at 60 $^\circ\text{C}$ under vacuum for 12 h to obtain TTA-BPY-COF.

2.3.2. Synthesis of Co-COF catalyst

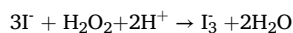
TTA-BPY-COF (20.00 mg) was immersed in 10 mL ethanol for ultrasonic dispersion. The suspension was bubbled under Ar atmosphere for 30 min. Next, $\text{Co}(\text{CH}_3\text{COO})_2 \cdot 4 \text{H}_2\text{O}$ (10.0 mg, 25 mmol) dissolved in 10 mL ethanol was slowly added to the above system, and continued to be bubbled for 30 min. Then the reaction system was sealed and stirred at room temperature for 8 h. The floating solid was collected by centrifugation and washed with N, N-dimethylformamide, deionized water, and methanol repeatedly to ensure removal of residual metal ions until the filtrate became colorless. Finally, the production was dried at 60 $^\circ\text{C}$ under vacuum for 12 h to obtain Co-COF. Fe-COF was prepared by the same procedure, and the COF was modified with $\text{FeCl}_2 \cdot 4 \text{H}_2\text{O}$ (4.95 mg, 25 mmol).

2.3.3. Synthesis of Co-Fe-COF catalyst

Iron was in-situ introduced in a three-electrode electrochemical cell: A solution with water (1 mL), isopropanol (0.25 mL), and Co-COF (6 mg) was sonicated for 30 min and evenly coated onto the FTO conductive glass (1 cm \times 1 cm) as working electrode. The electrochemical experiments were carried out in a three-electrode electrochemical cell, in which Pt electrode and calomel electrode were used as the counter electrode and reference electrode, respectively. $\text{FeSO}_4 \cdot 7 \text{H}_2\text{O}$ (0.1 M) was added into the electrolyte ratio of KCl (1 M) as electrolyte. Fe was introduced by continuously applying a voltage of 1.15 V (vs. RHE) for 2 hours. After the reaction, the floating solid was collected by centrifugation and washed thoroughly with ethanol (3×15 mL). The production was dried at 60 $^\circ\text{C}$ under vacuum for 12 h to obtain Co-Fe-COF.

2.3.4. Photocatalytic H_2O_2 production

A 300 W HX-F300XE lamp (Beijing NBET Technology Co. LTD.) equipped with UV cut-off ($\lambda > 420$ nm) was used for photocatalytic experiments. Typically, the sample (5 mg) and ultrapure water (15 mL) were dispersed by sonication. Before the photocatalytic reaction, the prepared solution was placed in a dark box, and the O_2 was bubbled through for 30 min to achieve O_2 saturation. For control experiments, bubble was performed with air and Ar instead of O_2 . The concentration of H_2O_2 was determined by iodometry. H_2O_2 can react with iodide ion (I^-) to produce triiodide ion (I_3^-) with strong absorbance at 350 nm according to the following chemical equation:



$$c(\text{H}_2\text{O}_2) = c(\text{I}_3^-)$$

Therefore, the H_2O_2 concentration can be obtained by measuring the I_3^- concentration. Typically, KI (0.4 M, 0.5 mL) aqueous solution was mixed with 0.5 mL of 0.1 M $\text{C}_8\text{H}_5\text{KO}_4$ (potassium hydrogen phthalate) aqueous solution. Add the sample solution (1 mL) to the mixture and hold for 45 minutes. The absorbance of the mixture at 350 nm was then measured using an ultraviolet-visible spectrophotometer. A standard curve was established by measuring the absorbance of several known concentrations of H_2O_2 solutions ($A = 0.01065 C - 0.01135$, $R^2 = 0.99959$).

2.3.5. Photodegradation experiment

An TC aqueous solution (50 mg/L) was prepared, and then the photocatalyst (5 mg) was added into the prepared solution (50 mL) and ultrasonicated for 5 min under dark. And then the above system was stirred for 60 min to reach adsorption equilibrium. Photocatalytic degradation experiments were performed by utilizing a xenon lamp ($\lambda \geq 420$ nm). The supernatant was extracted with a 0.22micron membrane filter every 2 mins, and then the sample was measured with an ultraviolet spectrophotometer. The catalyst was washed with ethanol and dried, and the recyclability degradation test was carried out (the same as the degradation process of other pollutants)

3. Results and discussion

3.1. Preparation and structural characterization

The combination of Co-Fe heteroatom pairs on the pore walls of TTA-BPY-COF proceeds through a two-step reaction. Co(II) was introduced into the COF structure by impregnation-assisted coordination method. Subsequently, Fe(II) was introduced into the ortho position of Co atom via in-situ electrochemical introduction (Fig. 1a). Powder X-ray diffraction (PXRD) patterns confirmed the high crystallinity and phase purity of the synthesized COF (Fig. 1b). A prominent diffraction peak at 2.39° could be observed, which corresponds to (100) crystal facets on AA layer stack, which indicated the presence of a well-organized long-range structure. And other diffraction peaks were also in good agreement with the result of simulations. Fourier transform infrared (FT-IR) spectra was performed to investigate the characteristic functional groups of TTA-BPY-COF. Compared to the monomers, the N-H (3320 cm^{-1}) and C=O (1670 cm^{-1}) stretching peaks in TTA-BPY-COF disappeared, whereas there were hydrazone bond formations at 1618 cm^{-1} , 1510 cm^{-1} (Fig. 1c)[9,31], indicating the formation of hydrazone linkages. The Brunauer-Emmett-Teller (BET) surface area and pore volume of TTA-BPY-COF were calculated to be $308.774\text{ cm}^2\text{g}^{-1}$ and $0.347\text{ cm}^3\text{g}^{-1}$. In addition, the diameter distribution of these three catalysts was mainly concentrated in relatively narrow distribution, and the peak value determined by the NL-DFT method is about 2.9 nm (Fig. 1d, e), which match the analog value. Although the internal cavity of TTA-BPY-COF was partially blocked due to the introduction of Co-Fe heteroatom pairs, the open holes and structures still existed, ensuring the accessibility of reactants to metal catalytic sites during the catalytic process.

The scanning electron microscopy (SEM) and transmission electron

microscopy (TEM) images of TTA-BPY-COF revealed an assembly of irregular synaptic aggregation of nanomaterials regardless (Fig. 2a, b). In addition, high-resolution TEM (HRTEM) imaging further revealed the structural details of TTA-BPY-COF. The 2D layered structure with an interlayer distance of $\sim 3.6\text{ \AA}$ was observed (Fig. 2c). The selected area regional diffraction (SAED) pattern showed no diffraction spots (Fig. 2d). Aberration-corrected high-Angle annular dark-field scanning TEM (HAADF-STEM) was used to observe the atomic dispersion more intuitively. The individual bright spots represented Fe/Co atom because their atomic mass was greater than C and N. Due to the height and orderly pore structure of TTA-BPY-COF, uniformly separated decentralized Co single atoms were observed (Fig. 2e). Most of the highlights in Ce-Fe-COF were paired (typically circled), consequently named as Co-Fe hetero-atom pairs (Fig. 2f). The region at the edge of the sample most likely to be monolayer material was selected for analysis, which indicated that the distance between adjacent metal atoms was approximately 0.27 nm, confirming the existence of Co-Fe hetero-atom pairs (Fig. 2g, h), which was consistent with the theoretical model calculation. The EDS mapping images further revealed that Co and Fe were uniformly distributed throughout in the entire bone, rather than Co-COF and Fe-COF as two separate monometrically-based structures (Fig. 2i-m).

X-ray photoelectron spectroscopy (XPS) was carried out to reveal the status of Co/Fe in Co-Fe-COF. The survey spectrum confirmed the elemental compositions of Co-COF and Co-Fe-COF. The C 1s spectra of Co-COF and Co-Fe-COF displayed two characteristic peaks when 284.8 eV and 286.1 eV, which belonged to the C=C/C-C bond and C=N bond of COF, respectively. Importantly, the $\pi-\pi^*$ transition of electrons during X-ray irradiation leads to the existence of sp^2 satellite peaks in the metal-COF (Fig. 3a), which was strong evidence for the formation of extended π -conjugation after cyclization[15,27]. The high-resolution N 1s spectra of these precursors deconvoluted into Co were successfully introduced into the structure of TTA-BPY-COF. Compared to the TTA-BPY-COF, a slight shift of peak could be observed in N 1s spectrum of Co-COF, which was attributed to the successful introduction of Co in the pyridine N of TTA-BPY-COF (Fig. 3b)[32]. The XPS spectrum of O 1s exhibits two peaks at 532.28 eV, 535.58 eV, which are derived from oxygen atoms on the Co(Fe)-O and absorbed water (Fig. 3c)[33]. After the photocatalytic reaction, the characteristic peaks of C 1s, N 1s, and O 1s of metal-COF did not show obvious main peak shift, which further indicated that the skeleton was intact and decomposition did not occur. For Co 2p XPS (Fig. 3d), spikes near 777–784 eV and 793–801 eV are classified as divalent Co species [Co(II)][33]. Compared with the

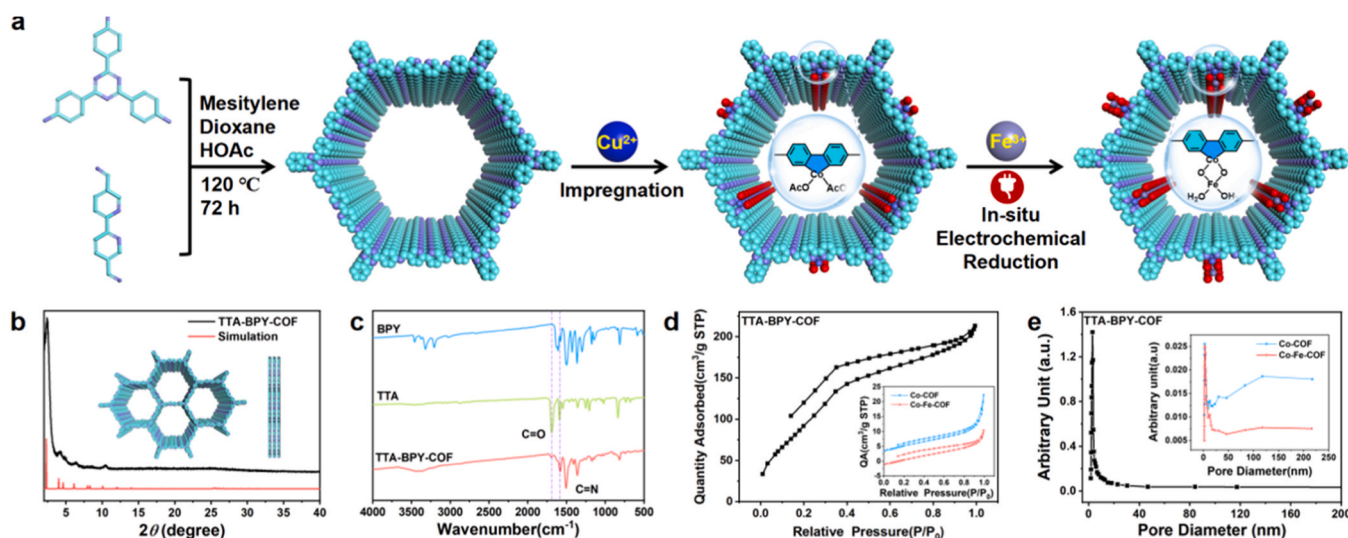


Fig. 1. Synthesis method and characterization. (a) Synthetic scheme of Co-Fe-COF, (b) Powder X-ray diffraction (PXRD) patterns of TTA-BPY-COF, (c) FTIR spectra of TTA-BPY-COF, (d) N_2 sorption isotherms at 77 K, and (e) Pore-size distribution profiles of TTA-BPY-COF, Co-COF, and Co-Fe-COF.

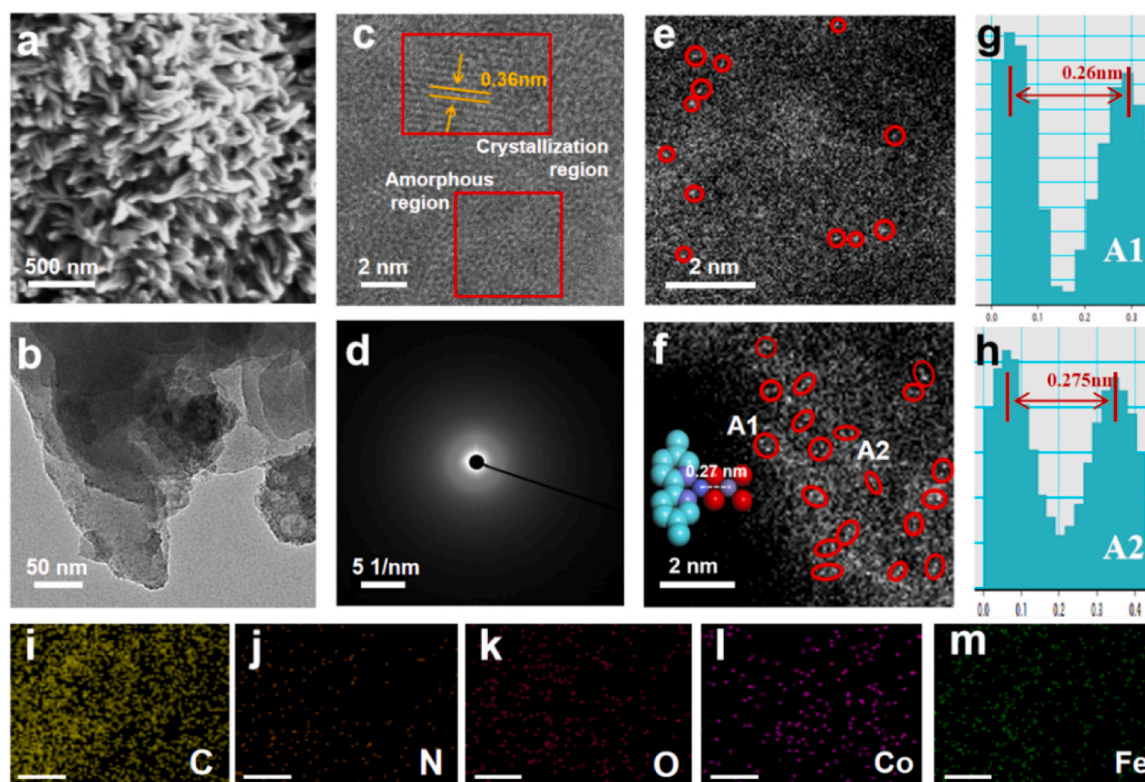


Fig. 2. Morphology. (a) SEM image of TTA-BPY-COF, (b, c) TEM image of TTA-BPY-COF, (d) SAED patterns (e) HAADF-STEM images of Co-CoF, (f) HAADF-STEM images of Co-Fe-COF, (g, h) The corresponding intensity distributions for A1 and A2 regions in Fig. 2f, EDS spectra of (i-m) Co-Fe-COF components were C, N, O, Co, Fe, respectively (The scale is 2 μm).

Co-CoF, the peak value of Co 2p in Co-Fe-COF can transfer to higher binding, suggesting that there is a synergistic interaction between Co and Fe after the introduction of Fe in the adjacent position of Co. The Co-Fe-COF package of XPS spectra showed the characteristics of binary oxidation state of Fe^{2+} species along with its associated satellite characteristics (Fig. 3e) [34]. In the displayed Fe 2p spectrum, the binding energies located at 708.58 eV ($\text{Fe}^{2+} 2p_{3/2}$), 719.18 eV ($\text{Fe}^{2+} 2p_{1/2}$), demonstrating that Fe mainly exists as Fe^{2+} species, which proved that there was no or minimal change of the oxidation state of metal species after being incorporated into the COF. According to previous work, Co^{2+} and Fe^{2+} interact with bridging O^{2-} via π -donation. When the electron cloud density of Co atoms has increased, there was a relatively weak e^-e^- repulsive force will appear between Co^{2+} and O^{2-} , strengthening the π -donation via Fe-O. Such a facilitated electron transfer process was also confirmed by O 1s XPS spectroscopy (Fig. 3b). In summary, Co-Fe-COF optimizes the synergistic effect between Co-Fe and accelerates the electron transfer process through the O^{2-} bridge. When Co is coordinated with Fe, part of the charge can be transferred from the Co site to the Fe site, and the self-healing cycle of Fe(II)/Fe(III) can be dynamically activated, which is conducive to the generation of $\bullet\text{OH}$, and can significantly promote the charge transfer between Co-Fe-COF and $\bullet\text{OH}$, thus optimizing the performance of OER.

To further disclose the surface structure and electronic properties of Fe and Co in Co-Fe-COF, X-ray absorption near edge spectroscopy (XANES) and extended X-ray absorption fine structure (EXAFS) analysis were performed. The near-edge absorption of Co-Fe-COF was close to that of CoO on the Co K-edge, and the absorption position was located between Co_3O_4 and Co foil, indicating that the valence of Co element was between 0 to +2.7 (Fig. 3f) [35]. Similarly, the valence state of Fe atoms in Co-Fe-COF ranged 0 to +3 (Fig. S13). The EXAFS spectra of Fe and Co indicate that there are significant differences in the local coordination of metal sites. The Co K-edge EXAFS spectra of CoPor, CoO and Co-Fe-COF had a main peak at $\sim 1.28 \text{ \AA}$, which ascribed to the Co-N/O

path (Fig. 3g) [36]. The Fe K-edge EXAFS spectra of Fe-O and Co-Fe-COF with the main peak at $\sim 1.49 \text{ \AA}$ attributed to the Fe-O path (Fig. 3h) [37]. It is noteworthy that the FT-EXAFS spectra of Co-Fe-COF all have a peak belonging to the Fe-Co bond, which is significantly distinct from Co-Co bond and Fe-Fe bond, confirming the existence of Co-Fe diatomic pairs (Fig. 3j, h). Wavelet transforms (WT)-EXAFS has also been utilized for the identification of metal-N/O and metal-metal paths (Fig. 3j). Both the Co and Fe K-edge WT-EXAFS spectra of Co-Fe-COF have a signal located at $\sim 7.4 \text{ \AA}^{-1}$, corresponding to the Co-Fe paths. This is significantly different from Co-Co bonds ($\sim 7.7 \text{ \AA}^{-1}$) and Fe-Fe bonds ($\sim 9.8 \text{ \AA}^{-1}$). The correlation between FT-EXAFS and WT-EXAFS signals confirms the presence of metal-N/O coordination bonds and Co-Fe bonds in Co-Fe-COF [38]. Additionally, the specific coordination configuration and structural parameters of each metal sites were investigated by quantitative least-squares EXAFS curve fitting method [39]. As depicted in Fig. 3i, the experimental results align closely with fitting parameters utilizing Co-Fe, Fe-O, and Co-O/N scattering routes (Table S1) [15]. This again supports the formation of Co-Fe heteroatom pairs, instead of metal-based nanoparticles.

3.2. Photoelectrochemical measurements

A series of photo electrochemistry characterization was carried out to study the light trapping ability and the dynamic behavior of photo-generated charge for Co-Fe-COF. The transient photocurrent response result showed that the maximum photocurrent density of Co-Fe-COF proves its most efficient photoelectric conversion efficiency (Fig. 4a). Steady-state photoluminescence (PL) spectra displayed that the peak intensity of Co-Fe-COF was significantly reduced compared with that of Co/Fe-COF (Fig. 4b). The times-resolved photoluminescence (TRPL) attenuation spectrum in Fig. 4c showed that the fluorescence lifetime of Co-Fe-COF package was higher than that of Co/Fe-COF package. The average fluorescence lifetime of Co-Fe-COF is 1.1136 ns, which was

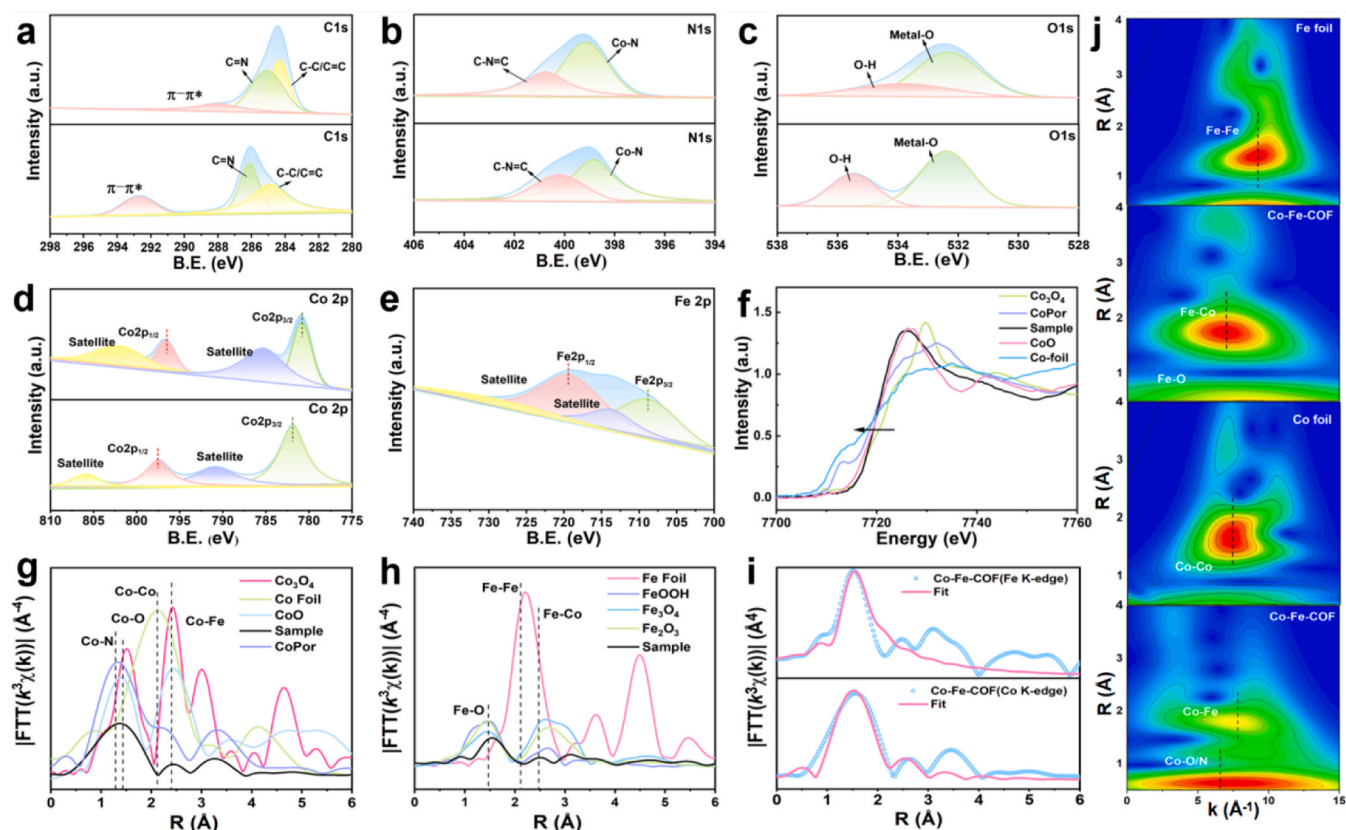


Fig. 3. The High-resolution (a) C 1s, (b) N 1s, (c) O 1s, (d) Co 2p and (e) Fe 2p XPS spectra in the Co-COF and Co-Fe-COF. (f) Co K-edge XANES spectra of the Co foil, Co_3O_4 , CoO, CoPor and Co-Fe-COF. FT-EXAFS spectra at Co K-edge (g) and Fe K-edge (h), respectively. The comparison of experimental EXAFS signals and simulation profile for Fe and Co (i), (j) WT-EXAFS spectra of Co-Fe-COF.

higher than that of Co/Fe-COF (Table S2)[40,41]. Lower PL peak intensity and higher lifetime of Co-Fe-COF imply higher charge separation efficiency, which may be due to the coupling of heteroatoms to Co-Fe to promote the transfer of TTA-BPY-COF photoelectrons to the active site.

UV-Vis diffuse reflectance spectroscopy (DRS) and Mott-Schottky diagram were used to study the photophysical properties and band structures of different photocatalysts, respectively. The positive sloping rate of the electrochemical Mott-Schottky plots indicated n-type semiconductor properties of photocatalysts. The flat band potential (Fig. 4d-f) was fitted to -0.42 V, -0.40 V, and -0.38 V (vs. Ag/AgCl) for Co-COF, Fe-COF, and Co-Fe-COF, respectively. The UV-vis DRS in visible range exhibited strong adsorption, and the band gaps of Co-COF, Fe-COF and Co-Fe-COF were calculated through the Tauc diagram to be 2.22 eV, 2.01 eV and 2.03 eV, respectively (Fig. 4g). Based on this, the corresponding conduction band (CB) and valence band (VB) were calculated (Fig. 4h)[10]. From the analysis of band gap structures, Co-Fe-COF possesses a moderate band gap, which is the closest to the energy level that can drive the synchronous reaction. This hetero-atomic pair Co-Fe-COF photocatalytic system had thermodynamically excellent separation of photogenerated electrons and pores. Electrochemical impedance spectroscopy (EIS) was employed to evaluate the electronic conductivity of photocatalysts. Co-Fe-COF exhibited the smallest radius of the front semicircles, which proved the minimum internal resistance of the interfacial charge transfer, further indicating the cooperation between Co and Fe can significantly enhance charge transfer (Fig. 4i). The results of atomic force microscopy (AFM) showed that the surface potential of the material has changed significantly before and after the application of light, demonstrating that the photogenerated charge and cavity separation process (Fig. 4j-l). All these optoelectronic chemical properties showed that the Co-Fe-COF is a kind of excellent photocatalyst.

3.3. Photocatalytic $\bullet\text{OH}$ production

Subsequently, the surface tandem reaction process of $\text{O}_2 + \text{H}_2\text{O} \rightarrow \text{H}_2\text{O}_2 \rightarrow \bullet\text{OH}$ over photocatalysts was analyzed in detail. The evaluation of photocatalytic H_2O_2 production over Co-COF photocatalyst was evaluated by UV-Vis spectroscopy with potassium hydrogen phthalate and potassium iodide as peroxide indicators. Irradiation without any sacrificial agent or cocatalyst was conducted in O_2 -saturated, air, and Ar atmospheres, respectively. It is evident that in the O_2 -saturated system, the photocatalytic H_2O_2 production over Co-COF maintains a consistently high level, surpassing that of the other atmospheres (Fig. 5a, b), indicating the essential role of O_2 and the key pathway of ORR in driving H_2O_2 generation in our system. The photocatalytic H_2O_2 generation experiments were also conducted over Fe-COF and Co-Fe-COF. The results demonstrated that Co-COF exhibits the highest yield, followed by Co-Fe-COF, while Fe-COF displayed the lowest yield. This can be attributed to the superior ORR capability of Co-COF compared with Fe-COF. And the significant loss of H_2O_2 observed in the Co-Fe-COF photocatalyst, which also proves the occurrence of the tandem catalytic reaction process involving $\text{O}_2 + \text{H}_2\text{O} \rightarrow \text{H}_2\text{O}_2 \rightarrow \bullet\text{OH}$ (Fig. 5c).

In-situ Fourier transform infrared spectroscopy (FT-IR) was used to investigate the intermediate pathway of $\bullet\text{OH}$ formation (Fig. 5d-g). Before conducting in-situ FT-IR measurements, the sample was placed inside an in-situ infrared tank and saturated with a continuous flow of high-purity O_2 through deionized water for 15 min, ensuring an absence of light during this process. Subsequently, the samples were subjected to testing for 10 minutes under the dark conditions as a control, followed by illumination with a light source for 50 minutes. Notably, only Co-Fe-COF exhibits a significant absorption band at approximately 3500 cm^{-1} corresponding to the $\bullet\text{OH}$ stretch $\nu(\text{H}_2\text{O})$ [42], which manifested upon

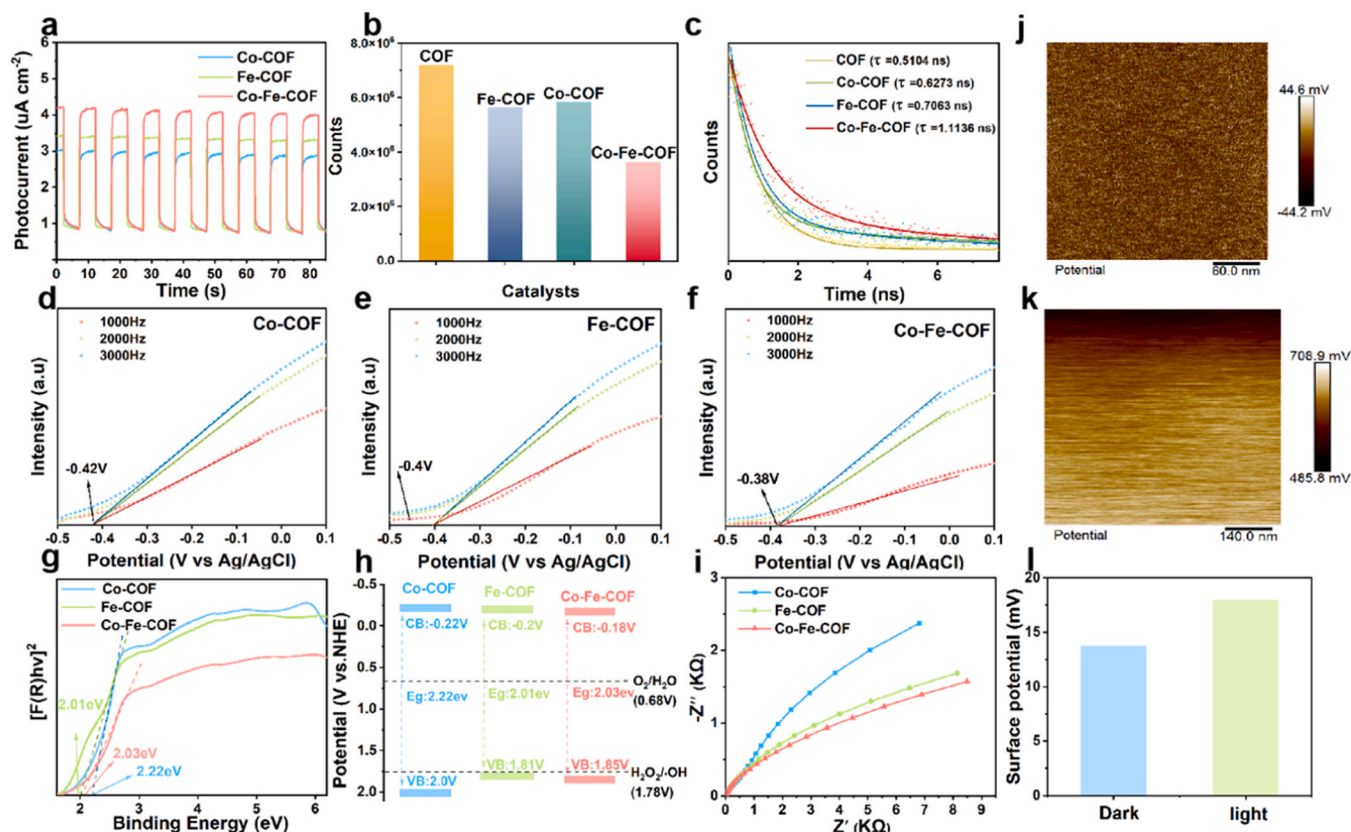


Fig. 4. Photochemical properties of Co-Fe-COF. (a) Transient photocurrent responses, (b) Steady-state photoluminescence (PL) spectrum, (c) Time-resolved photoluminescence attenuation spectrum, Mott-Schottky plots for (d) Fe-COF, (e) Co-COF, and (f) Co-Fe-COF. (g) Calculated optical band gap (Eg) based on the Kubelka–Munk transformed reflectance spectra of Metal-COF, and (h) Band gap. (i) electrochemical impedance spectra (EIS), (j–l) Atomic force microscope (AFM).

exposure to light and gradually intensified over time. Simultaneously, in-situ FT-IR was utilized to identify intermediates involved in $\bullet\text{OH}$ formation (Fig. 5h)[43]. The band near 1419 cm^{-1} can be attributed to the O-O stretching vibration caused by adsorption of O_2 molecules on the surface of Co-COF, which is a prerequisite for ORR. In addition, with increasing illumination time on Co-COF, two distinct bands emerged and grew stronger: one centered around 1178 cm^{-1} representing $\bullet\text{OOH}$ species associated with surface adsorption and another weaker band at approximately 1329 cm^{-1} indicating $\bullet\text{H}_2\text{O}_2$ bending mode also related to surface adsorption. The results confirmed the presence of $\bullet\text{OOH}$ and $\bullet\text{H}_2\text{O}_2$ intermediates during light-driven tandem catalytic reaction. Finally, electron paramagnetic resonance (EPR) spectra were obtained under dark and visible light irradiation using 5,5-dimethyl-1-pyrrolin-N-oxide (DMPO) as the trapping agent. As shown in Fig. 5i, under the simulated sunlight irradiation, Co-Fe-COF showed four-fold stronger peaks (four peaks with intensity of 1:2:2:1) than the Co-COF[44].

3.4. DFT calculations

Subsequently, the active site and the reaction mechanism were investigated through DFT calculation. The adsorption configuration of O_2 determines the reaction pathway of H_2O_2 generation. Therefore, we compared the adsorption energies of different O_2 adsorption configurations on surfaces of Co-Fe-COF (Fig. 6a). The results show that the end-on type adsorption configuration of O_2 is preferential to form on Co-Fe-COF site. The charge-density difference map further unveils that the coupling synergy between heteroatom pairs results in significant charge transfer at the Co site to the adsorbed O_2 (Fig. 6b,c, e,f). The partial density of states (PDOS) shows that the d-band center of Co-Fe-COF is closer to the Fermi level than that of Co-COF, indicating stronger adsorption between O_2 and Co site (Fig. 6d). The second stage of the

tandem-catalytic reaction was the Fenton reaction. The DFT results show that the O-O distance on the generated H_2O_2 is stretched as it transfers to the Fe site (Fig. 6g). Correspondingly, the Gibbs free energy (ΔG) for each step involved in $2e^-$ ORR and Fenton reaction was calculated, as shown in Fig. 6h. Efficient generation of $\bullet\text{OH}$ depends on both selective H_2O_2 generation and the cleavage of H_2O_2 into $\bullet\text{OH}$, so the two binding energies of $\bullet\text{OOH}$ and $\bullet\text{H}_2\text{O}_2$ are crucial. According to the reported volcanic relationship between $\bullet\text{OOH}$ and dual-electron ORR properties, moderate $\bullet\text{OOH}$ binding favors selective catalytic H_2O_2 generation. The $\bullet\text{OOH}$ ($\text{O}_2 + \text{H}^+ + e^- \rightarrow \bullet\text{OOH}$) ΔG value of Co-Fe-COF is 0.48 eV , which is lower than the $\Delta G^{\bullet\text{OH}}$ value of Co-Fe-COF (0.52 eV), indicating that the O_2 adsorbate by Co-Fe-COF is more easily activated into $\bullet\text{OOH}$ (Fig. 6h). Moreover, as shown in Fig S15, $\bullet\text{OOH}$ binds to Co-Fe-COF, making $\bullet\text{O}_2$ uphill towards $\bullet\text{OOH}$, and the energy barrier is 0.48 eV , lower than 0.59 eV at the Co-COF site, indicating that the O-bridged Co-Fe hetero-pairs have high H_2O_2 selectivity. Furthermore, the adsorption of H_2O_2 on Fe site was a downhill process which is more thermodynamically favorable (Fig. 6i). The results suggest that the activation enhancement of H_2O_2 at the Fe site may be due to the electron donation of the adjacent Co site through the O-bridge, thus facilitating self-healing from Fe(III) to Fe(II). By coupling the Co and Fe activated sites, the two-step combination energy of $\bullet\text{OOH}$ and $\bullet\text{H}_2\text{O}_2$ in ORR can be simultaneously optimized to achieve selective generation of H_2O_2 and efficient reduction of H_2O_2 to $\bullet\text{OH}$. It is proposed that the $\bullet\text{OH}$ electro generation via ORR on Co-Fe-COF is as follows: First of all, in the two consecutive electronic paths, the electron transitions to the metal, and O_2 is preferentially adsorbed on the Co site rather than the Fe site that is conducive to catalyzing O-O cleavage (\bullet denotes the active site). $\bullet\text{O}_2$ is subsequently reduced to $\bullet\text{H}_2\text{O}_2$ at the Co site by $\bullet\text{OOH}$ intermediates; since $\bullet\text{H}_2\text{O}_2$ has a strong combination with the Fe site, $\bullet\text{H}_2\text{O}_2$ may migrate to the Fe site and the final product is reduced to

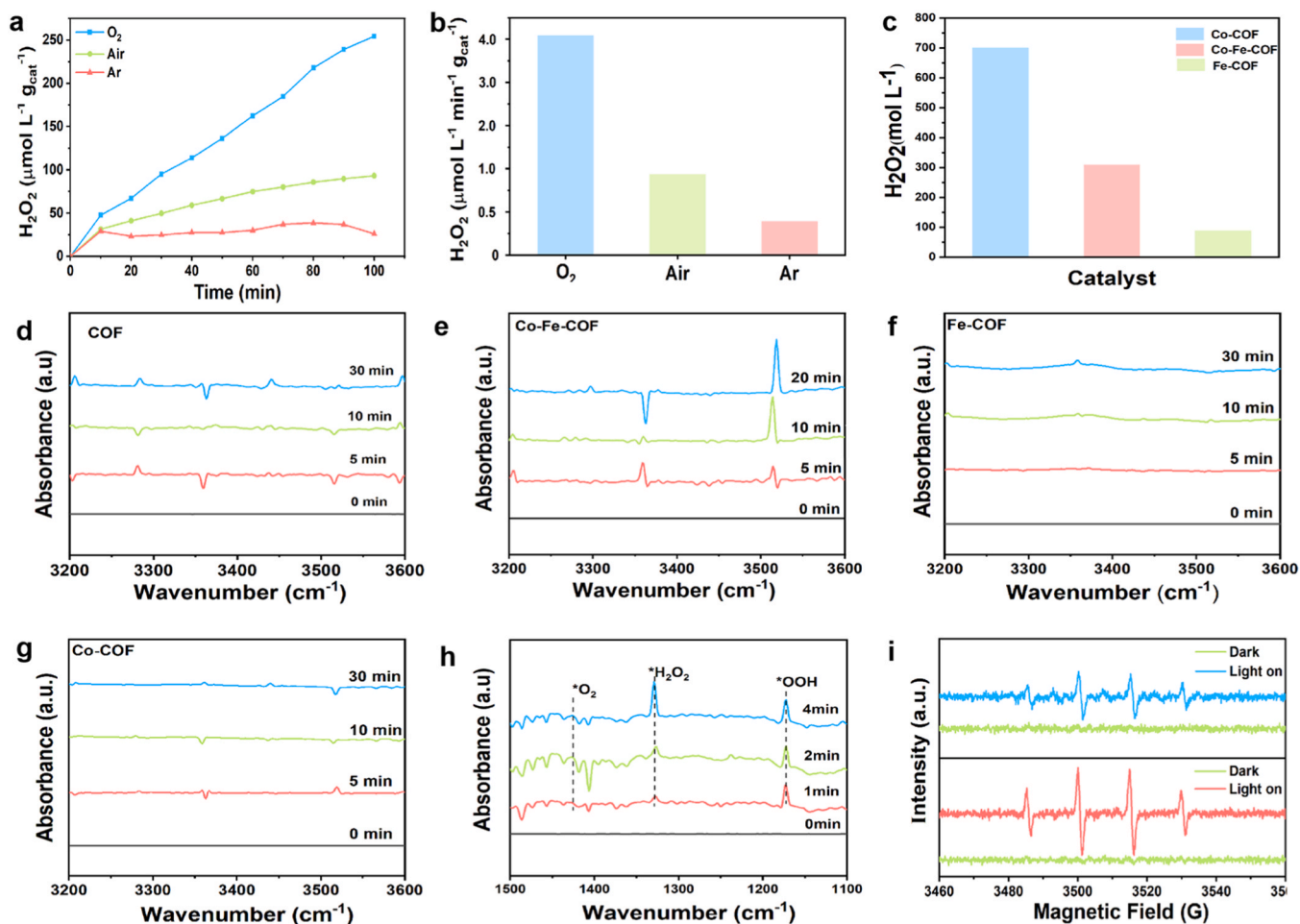


Fig. 5. Generation and detection of ROS on Co-COF, Fe-COF and Co-Fe-COF. (a) Photocatalytic H_2O_2 production of Co-COF, (b) H_2O_2 production in different gas atmospheres, (c) Comparison of photocatalytic H_2O_2 production performance of Co-COF with other photocatalysts. In situ FT-IR spectra vs illumination time for the photocatalytic system of (d) COF, (e) Co-COF, (f) Fe-COF and (g) Co-Fe-COF. (h) In situ FT-IR spectra recorded by the Co-COF in O_2 -saturated solution. (i) EPR spectra of COF obtained in the presence of DMPO as an electron-trapping agent.

•OH. Therefore, the efficient •OH photoreduction on Co-Fe-COF is achieved through the Co-catalysis of Co-Fe hetero-atomic pair (Fig. 6j, k).

3.5. Pollutant degradation

Environmental pollutants and Emerging contaminants (ECs) pose a global challenge as they impact the “One Health” concept [45]. In this study, tetracycline (TC), ciprofloxacin (CF), and bisphenol A (BPA) as representative new contaminants were chosen to the photocatalytic activity of as-synthesized photocatalysts. Prior to the experiment, the photocatalyst was introduced into the wastewater system and stirred in darkness for 30 minutes to achieve the adsorption-desorption equilibrium. It can be seen that in the dark, there was minimal reduction in tetracycline. Under light exposure, as shown in Fig. 7a, after 60 minutes, the degradation rate of tetracycline by Co-Fe-COF reached 79.82 %. Compared with TTA-BPY-COF, Co-COF and Fe-COF, the COF degradation effect of single metal was slightly improved, but the bimetal co-degradation effect was greatly improved, which was much higher than that of other catalysts. The degradation process of organic matter typically follows a first order reaction. Kinetic data of degradation were fitted, where c and k were tetracycline concentration and rate constants. Compared to TTA-BPY-COF and Co-COF, the degradation rates of tetracycline increased by 7.86 times and 4.53 times respectively (Fig. 7d). In order to verify the universality of Co-Fe-COF application,

ciprofloxacin and bisphenol A were subsequently selected for experiments (Fig. 7bc, ef). It can be seen that the degradation performance of Co-Fe-COF is still greatly improved compared with pure COF and COF with added single metal. The degradation rate of ciprofloxacin was 80.46 %, which was 4.4 times that of Co-COF. The degradation rate of bisphenol A was 89.93 %, 2.7 times that of Co-COF. Reusability is one of the main issues of evaluating the performance of the catalyst. In this study, five cycles of Co-Fe-COF were tested, and after five tests, the catalyst still maintained good degradation efficiency for the three pollutants. These all prove that composite materials enhance the optical activity (Fig. 7g-i).

In order to further investigate the potential of Co-Fe-COF in catalysts, a device-level demonstration was also designed to investigate the practical application of Co-Fe-COF in continuous wastewater degradation, as shown in Fig. 8. Compared with decentralized catalyst suspensions, membrane technology was sustainable and convenient, creating bright prospects for the supply of clean water resources. Co-Fe-COF membrane was prepared by placing Co-Fe-COF suspension on PVDF substrate (PVDF/Co-Fe) by vacuum assisted filtration method (Fig. 8d, e), the Co-Fe-COF membranes was flexible and elastic. Co-Fe-COF's abundant nano-pores can be used as an effective water transport channel, providing a completely active catalytic site for the rapid penetration and purification of wastewater (Fig. 8a). As shown in Fig. 8b and c, the methylene blue could be removed to almost 100 %. The Co-Fe-COF photocatalyst showed good stability in the degradation performance of

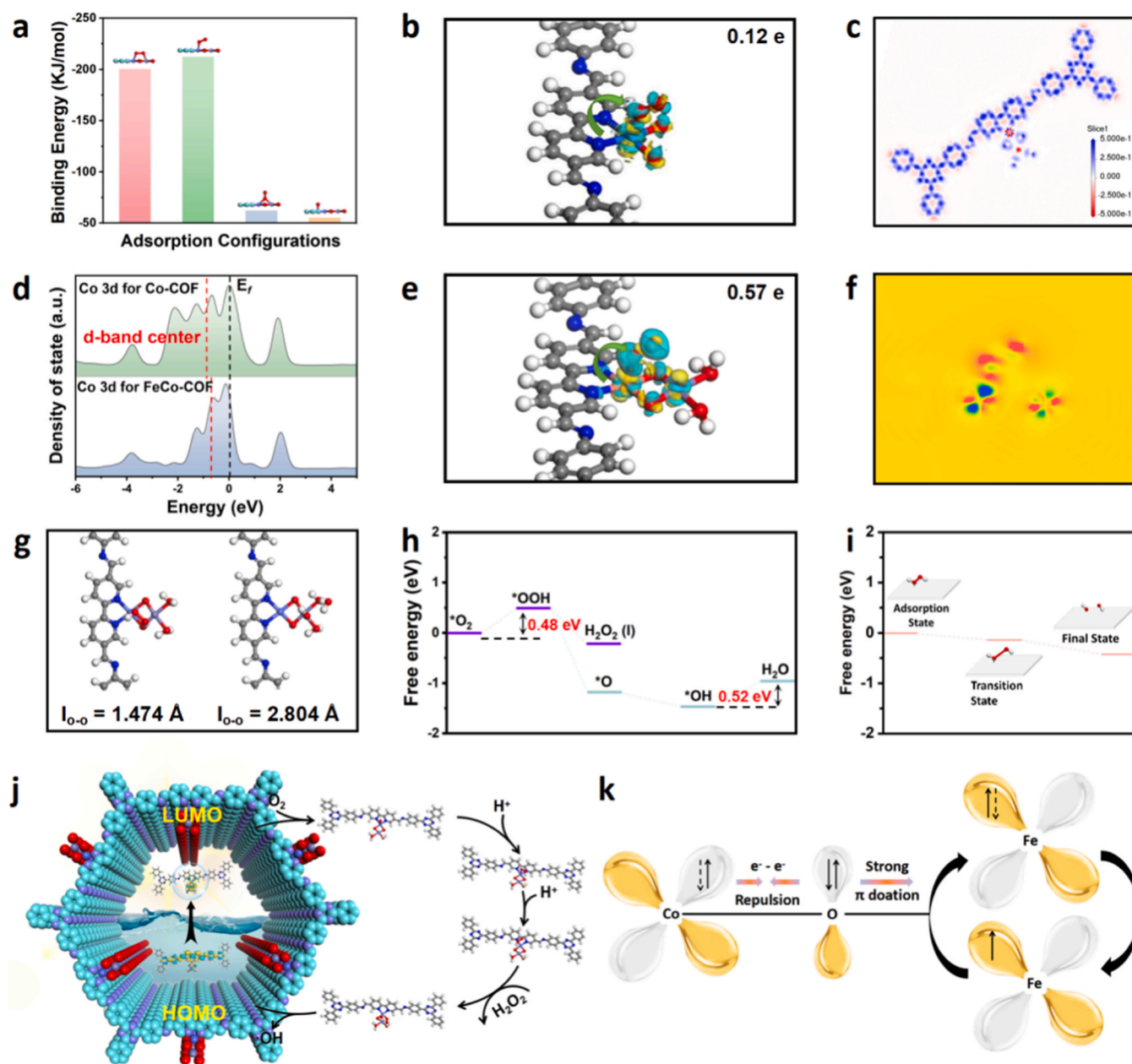


Fig. 6. DFT calculations and Mechanism. (a) Adsorption energy of O_2 adsorption configuration on the surface of Co-Fe-COF, (b) single-atom differential charge density diagram, (c) diatomic differential charge density diagram, section density distribution diagram (c) and side density distribution diagram (f) of Co-Fe-COF. (d) D-band center, (g) H_2O_2 reacts at the iron site, (h) Gibbs free energy diagram of reduction of O_2 and water to hydroxyl group on Co-Fe-COF. (i) Key steps of $\bullet\text{OH}$ production at Fe site, (j, k) The schematic diagram of photocatalytic $\bullet\text{OH}$ production for the Co-Fe-COF.

methylene blue under continuous water circulation.

4. Conclusion

In conclusion, a novel O-bridged Co-Fe hetero-atom pair tandem photocatalyst has been precisely constructed by employing different in-situ introduction strategies of Co and Fe on the COF pore wall. The detailed conformational and coordination structures of the heteroatom pair Co-Fe were revealed by AHAADF-STEM and EXAFS. Experimental results demonstrate that the as-synthesized Co-Fe-COF presents highly efficient hydroxyl radicals production following the process of $\text{O}_2 + \text{H}_2\text{O} \rightarrow \text{H}_2\text{O}_2 \rightarrow \bullet\text{OH}$. Additionally, the assembly of Co-Fe hetero-atom pairs on the periodic pore walls of COF can significantly boost the enrichment capacity for contaminant molecules, thus further improving the utilization rate of $\bullet\text{OH}$, thus exhibiting excellent degradation

efficiency for various refractory organic pollutants. Theoretical simulations reveal that the proximity electronic effect of O-bridged Co-Fe thermodynamically not only is beneficial to the formation of OOH^* intermediate, but also dynamically facilitates electronic transformation from Co to Fe, which activates the self-healing cycle of Fe(II)/Fe(III) . This study offers a new approach for designing high-performance tandem catalysts.

CRediT authorship contribution statement

Xu Wu: Supervision, Project administration, Funding acquisition. **Ruijuan Bian:** Validation. **Ruoyun Gao:** Supervision. **Pengfei Li:** Validation, Supervision, Formal analysis. **Yang Deng:** Writing – review & editing, Supervision, Software, Funding acquisition. **Yali Luo:** Writing – original draft, Methodology, Investigation, Data curation,

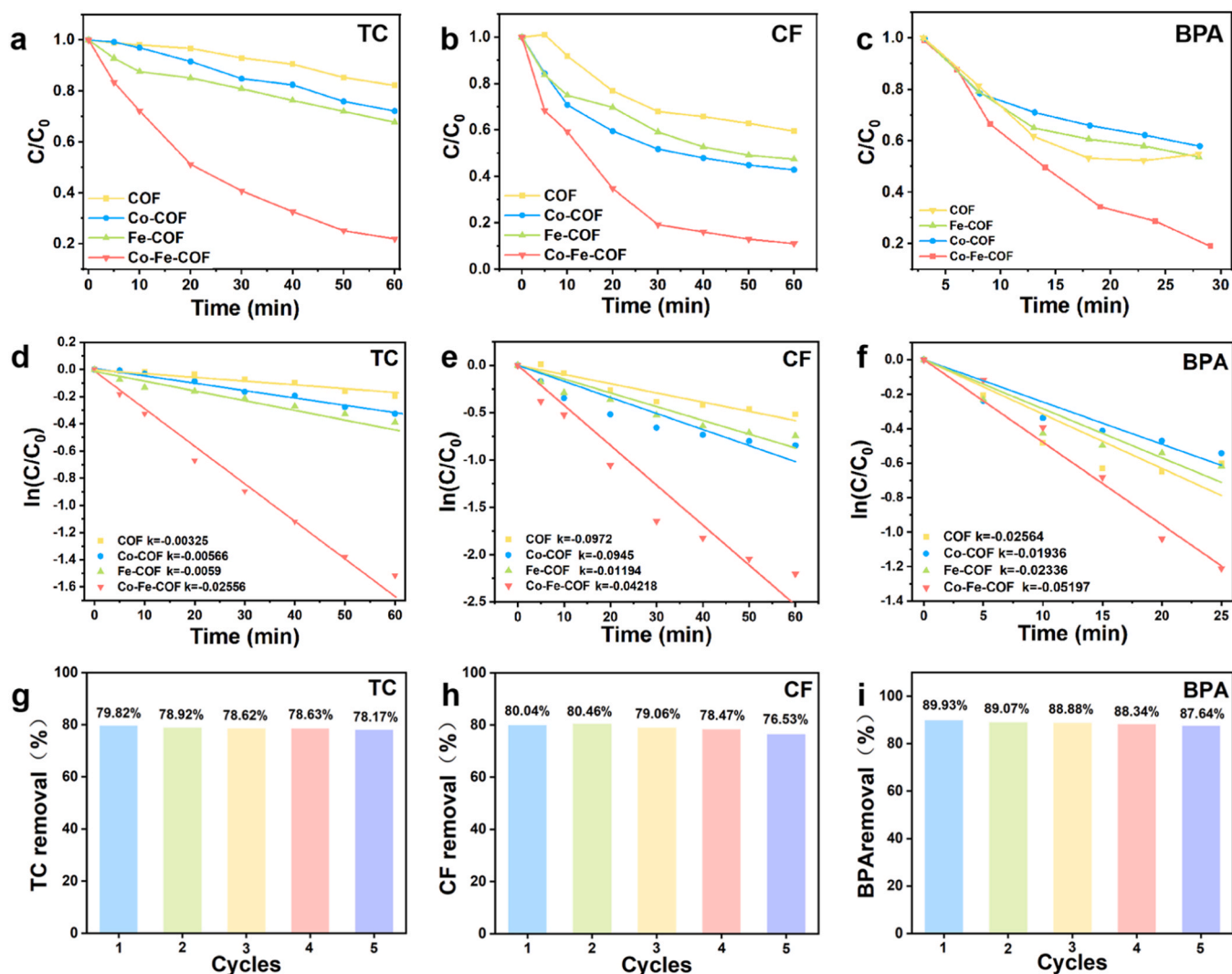


Fig. 7. Photocatalytic performances of Co-Fe-COF as a Fenton reagent. Degradation of TC, CF and BPA in the Co-Fe-COF system, the inset image shows the curves of organic pollutant removal fitted by first-order and the pseudo-first-order reactions (a-f). Cyclic degradation of organic pollutants in Co-Fe-COF system(g-i).

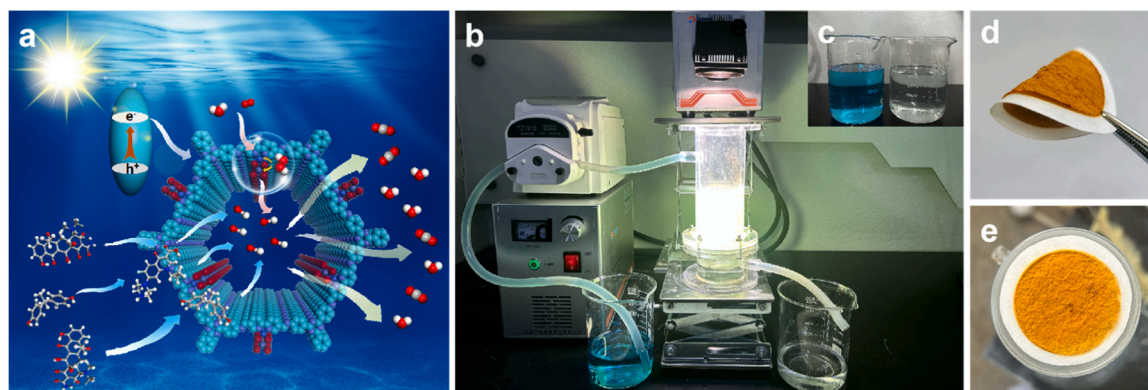


Fig. 8. Preparation of Co-Fe-COF membrane by continuous flow system and its application in water treatment. (a) Cyclic water photodegradation simulation. (b) Photocatalytic wastewater treatment experimental equipment diagram. As a proof of concept, methylene blue was used as a degradant to better observe the degradation effect. (c) Before and after degradation. (d), (e) front and side photos of the prepared Co-Fe-COF, the membrane has high flexibility.

Conceptualization.

Declaration of Competing Interest

The authors declare that they have no known competing financial interests or personal relationships that could have appeared to influence

the work reported in this paper.

Data Availability

Data will be made available on request.

Acknowledgements

This work was supported by the National Natural Science Foundation of China (22272116). Youth Science Foundation of Shanxi Province (202303021212034). The authors would like to thank Shiyanjia Lab (www.shiyanjia.com) for the support of TEM test.

Appendix A. Supporting information

Supplementary data associated with this article can be found in the online version at [doi:10.1016/j.apcatb.2024.124255](https://doi.org/10.1016/j.apcatb.2024.124255).

References

- [1] T. Zhang, Y. Wen, Z. Pan, Y. Kuwahara, K. Mori, H. Yamashita, Y. Zhao, X. Qian, Overcoming acidic $\text{H}_2\text{O}_2/\text{Fe(II/III)}$ redox-induced low H_2O_2 utilization efficiency by CarbonQuantum dots Fenton-like catalysis, *Environ. Sci. Technol.* 56 (2022) 2617–2625.
- [2] R.A. Borse, Y.X. Tan, J. Lin, E. Zhou, Y. Hui, D. Yuan, Y. Wang, Coupling electron transfer and redox site in boron covalent organic framework toward boosting photocatalytic water oxidation, *Angew. Chem. Int. Ed.* 63 (2024) e202318136.
- [3] Y. Shi, X. Wang, X. Liu, C. Ling, W. Shen, L. Zhang, Visible light promoted Fe_3S_4 Fenton oxidation of atrazine, *Appl. Catal. B: Environ.* 277 (2020) 118643.
- [4] X. Zhang, J. Tang, L. Wang, C. Wang, L. Chen, X. Chen, J. Qian, B. Pan, Nanoconfinement-triggered oligomerization pathway for efficient removal of phenolic pollutants via a Fenton-like reaction, *Nat. Commun.* 15 (2024) 917.
- [5] L. Qin, J. Meng, G. Yang, Y. Pan, X. Gao, Y. Yang, Y. Guo, Interlayer single-atomic Fe–N4 sites on carbon-rich graphitic carbon nitride for notably enhanced photo-Fenton-like catalytic oxidation processes towards recalcitrant organic micropollutants, *Appl. Catal. B: Environ.* 345 (2024) 123695.
- [6] Y. Shi, G. Zhang, C. Xiang, C. Liu, J. Hu, J. Wang, R. Ge, H. Ma, Y. Niu, Y. Xu, Defect-engineering-mediated long-lived charge-transfer excited-state in Fe-gallate complex improves iron cycle and enables sustainable fenton-like reaction, *Adv. Mater.* 36 (2024) e2305162.
- [7] J. Xiong, X. Li, J. Huang, X. Gao, Z. Chen, J. Liu, H. Li, B. Kang, W. Yao, Y. Zhu, CN/rGO@BPQDs high-low junctions with stretching spatial charge separation ability for photocatalytic degradation and H_2O_2 production, *Appl. Catal. B: Environ.* 266 (2020) 118602.
- [8] Q. Liao, D. Wang, C. Ke, Y. Zhang, Q. Han, Y. Zhang, K. Xi, Metal-free Fenton-like photocatalysts based on covalent organic frameworks, *Appl. Catal. B: Environ.* 298 (2021) 120548.
- [9] Z. Zhou, M. Sun, Y. Zhu, P. Li, Y. Zhang, M. Wang, Y. Shen, A thioether-decorated triazine-based covalent organic framework towards overall H_2O_2 photosynthesis without sacrificial agents, *Appl. Catal. B: Environ.* 334 (2023) 122862.
- [10] J.N. Chang, Q. Li, J.W. Shi, M. Zhang, L. Zhang, S. Li, Y. Chen, S.L. Li, Y.Q. Lan, Oxidation-reduction molecular junction covalent organic frameworks for full reaction photosynthesis of H_2O_2 , *Angew. Chem. Int. Ed.* 62 (2023) e202218868.
- [11] X. Li, J. Xiong, X. Gao, J. Ma, Z. Chen, B. Kang, J. Liu, H. Li, Z. Feng, J. Huang, Novel BP/BiOBr S-scheme nano-heterojunction for enhanced visible-light photocatalytic tetracycline removal and oxygen evolution activity, *J. Hazard. Mater.* 387 (2020) 121690.
- [12] R. Ren, X. Shang, Z. Song, C. Li, Z. Wang, F. Qi, A. Ikhlaiq, J. Kumirska, E. Maria Siedlecka, O. Ismailova, Active electronic structure derived by Fe-Cl-C coordination of single-atom cathode applied in antibiotics degradation by electro-Fenton: Enhanced transformation of oxygen to hydroxyl radicals via 3-electron pathway, *Chem. Eng. J.* 474 (2023) 145545.
- [13] H. Liu, P. Zhu, D. Yang, C. Zhong, J. Li, X. Liang, L. Wang, H. Yin, D. Wang, Y. Li, Pd-Mn/NC dual single-atomic sites with hollow mesopores for the highly efficient semihydrogenation of phenylacetylene, *J. Am. Chem. Soc.* 146 (2024) 2132–2140.
- [14] D. Yu, Y. Ma, F. Hu, C.C. Lin, L. Li, H.Y. Chen, X. Han, S. Peng, Dual-sites coordination engineering of single atom catalysts for flexible metal–air batteries, *Adv. Energy Mater.* 11 (2021) 2101242.
- [15] Y. Zhou, Y. Liu, Z. Wang, C. Li, Z. Wang, S. Zhang, C. Deng, Fe-Co dual atomic doublets on N, P codoped carbon as active sites in the framework of heterostructured hollow fibers towards high-performance flexible Zn-Air battery, *Energy Storage Mater.* 59 (2023) 102772.
- [16] Y. Chen, J. Lin, Q. Pan, X. Liu, T. Ma, X. Wang, Inter-metal interaction of dual-atom catalysts in heterogeneous catalysis, *Angew. Chem. Int. Ed.* 62 (2023) e202306469.
- [17] L. Lei, X. Guo, X. Han, L. Fei, X. Guo, D.G. Wang, From synthesis to mechanisms: in-depth exploration of the dual-atom catalytic mechanisms toward oxygen electrocatalysis, *Adv. Mater.* (2024) e2311434.
- [18] P. Guo, B. Liu, F. Tu, Y. Dai, Z. Zhang, Y. Xia, M. Ma, Y. Zhang, L. Zhao, Z. Wang, Breaking Sabatier's vertex via switching the oxygen adsorption configuration and reaction pathway on dual active sites for acidic oxygen reduction, *Energy Environ. Sci.* (2024) 3077–3087.
- [19] W. Li, S. Xia, Z. Wang, B. Zhang, B. Li, L. Zhang, K. Qian, J. Ma, X. He, Covalency competition triggers Fe-Co synergistic catalysis for boosted Fenton-like reactions, *Appl. Catal. B: Environ.* 325 (2023) 122358.
- [20] J. Wang, Q. Zhang, F. Deng, X. Luo, D.D. Dionysiou, Rapid toxicity elimination of organic pollutants by the photocatalysis of environment-friendly and magnetically recoverable step-scheme $\text{SnFe}_2\text{O}_4/\text{ZnFe}_2\text{O}_4$ nano-heterojunctions, *Chem. Eng. J.* 379 (2020) 122264.
- [21] Y. Yue, P. Cai, K. Xu, H. Li, H. Chen, H.C. Zhou, N. Huang, Stable bimetallic polyphthalocyanine covalent organic frameworks as superior electrocatalysts, *J. Am. Chem. Soc.* 143 (2021) 18052–18060.
- [22] Y. Yusran, H. Li, X. Guan, Q. Fang, S. Qiu, Covalent organic frameworks for catalysis, *Energy Chem.* 2 (2020) 100035.
- [23] Q. Zheng, X. Li, Q. Zhang, D. Lee, H. Mao, C. Yang, K.C. Bustillo, J.A. Reimer, Y. Liu, J. Jiang, H. Zheng, A covalent organic framework onion structure, *Mater* 60 (2022) 98–105.
- [24] S.S.A. Shah, M.S. Javed, T. Najam, M.A. Nazir, A. ur Rehman, A. Rauf, M. Sohail, F. Verpoort, S.-J. Bao, Covalent organic frameworks (COFs) for heterogeneous catalysis: recent trends in design and synthesis with structure-activity relationship, *Mater* 67 (2023) 229–255.
- [25] L. Qin, C. Ma, J. Zhang, T. Zhou, Structural motifs in covalent organic frameworks for photocatalysis, *Adv. Funct. (2024)* 2401562.
- [26] Z. Meng, K.A. Mirica, Covalent organic frameworks as multifunctional materials for chemical detection, *Chem. Soc. Rev.* 50 (2021) 13498–13558.
- [27] N. Liu, J. Wei, J. Xu, Y. Yu, J. Yu, Y. Han, K. Wang, J.L. Oregre, Q. Ge, J. Sun, Elucidating the structural evolution of highly efficient Co-Fe bimetallic catalysts for the hydrogenation of CO_2 into olefins, *Appl. Catal. B: Environ.* 328 (2023) 122476.
- [28] X. Li, B. Kang, F. Dong, Z. Zhang, X. Luo, L. Han, J. Huang, Z. Feng, Z. Chen, J. Xu, B. Peng, Z.L. Wang, Enhanced photocatalytic degradation and $\text{H}_2/\text{H}_2\text{O}_2$ production performance of S-pCN/WO₂.72 S-scheme heterojunction with appropriate surface oxygen vacancies, *Nano. Energy* 81 (2021) 105671.
- [29] C. Chen, M. Sun, F. Zhang, H. Li, M. Sun, P. Fang, T. Song, W. Chen, J. Dong, B. Rosen, P. Chen, B. Huang, Y. Li, Adjacent Fe site boosts electrocatalytic oxygen evolution at Co site in single-atom-catalyst through a dual-metal-site design, *Energy Environ. Sci.* 16 (2023) 1685–1696.
- [30] X. Li, J. Liu, J. Huang, C. He, Z. Feng, Z. Chen, L. Wan, F. Deng, All organic S-scheme heterojunction PDI-Ala/S-C₃N₄ photocatalyst with enhanced photocatalytic performance, *Acta Phys. -Chim. Sin.* 37 (6) (2021) 2010030.
- [31] W. Gao, Y. Jian, Y. Li, C. Pan, G. Yu, J. Tang, Insight into the enhanced photo-fenton degradation performance of $\text{Fe}_3\text{O}_4/\beta$ -ketoenamine-linked covalent organic framework, *Ind. Eng. Chem. Res.* 62 (2023) 1891–1898.
- [32] D. Wang, F. Le, J. Lv, X. Yang, X. Chen, H. Yao, W. Jia, Fe-incorporated nickel-based bimetallic metal-organic frameworks for enhanced electrochemical oxygen evolution, *Molecules* 28 (2023) 4366.
- [33] X. Yang, X. Li, M. Liu, S. Yang, Q. Xu, G. Zeng, Confined synthesis of dual-atoms within pores of covalent organic frameworks for oxygen reduction reaction, *Small* 20 (2024) e2306295.
- [34] J. Ma, Q. Yang, Y. Wen, W. Liu, Fe-g-C₃N₄/graphitized mesoporous carbon composite as an effective Fenton-like catalyst in a wide pH range, *Appl. Catal. B: Environ.* 201 (2017) 232–240.
- [35] M. Liu, N. Li, S. Cao, X. Wang, X. Lu, L. Kong, Y. Xu, X.H. Bu, A "pre-constrained metal twins" strategy to prepare efficient dual-metal-atom catalysts for cooperative oxygen electrocatalysis, *Adv. Mater.* 34 (2022) e2107421.
- [36] H. Yang, F. Li, S. Zhan, Y. Liu, W. Li, Q. Meng, A. Kravchenko, T. Liu, Y. Yang, Y. Fang, L. Wang, J. Guan, I. Furó, M.S.G. Ahlquist, L. Sun, Intramolecular hydroxyl nucleophilic attack pathway by a polymeric water oxidation catalyst with single cobalt sites, *Nat. Catal.* 5 (2022) 414–429.
- [37] L. Ran, Z. Li, B. Ran, J. Cao, Y. Zhao, T. Shao, Y. Song, M.K.H. Leung, L. Sun, J. Hou, Engineering single-atom active sites on covalent organic frameworks for boosting CO_2 photoreduction, *J. Am. Chem. Soc.* 144 (2022) 17097–17109.
- [38] X. Li, X. Wen, J. Lang, Y. Wei, J. Miao, X. Zhang, B. Zhou, M. Long, P.-J.J. Alvarez, L. Zhang, CoN₁O₂ single-atom catalyst for efficient peroxymonosulfate activation and selective cobalt (IV)=O generation, *Angew. Chem. Int. Ed.* 62 (2023) e202303267.
- [39] Z. Jin, M. Yang, Y. Dong, X. Ma, Y. Wang, J. Wu, J. Fan, D. Wang, R. Xi, X. Zhao, T. Xu, J. Zhao, L. Zhang, D.J. Singh, W. Zheng, X. Cui, Atomic dispersed heteropairs for enhanced electrocatalytic CO_2 reduction, *Nano-Micro Lett.* 16 (2023) 4.
- [40] S. Shen, X. Li, Y. Zhou, L. Han, Y. Xie, F. Deng, J. Huang, Z. Chen, Z. Feng, J. Xu, F. Dong, Novel BiOBr/Bi₂S₃ high-low junction prepared by molten salt method for boosting photocatalytic degradation and H_2O_2 production, *J. Mater. Sci. Technol.* 155 (2023) 148–159.
- [41] L. Xiao, W. Ren, S. Shen, M. Chen, R. Liao, Y. Zhou, X. Li, Enhancing photocatalytic hydrogen evolution through electronic structure and wettability adjustment of ZnIn₂S₄/Bi₂O₃ S-scheme heterojunction, *Acta Phy-Chim. Sin.* 40 (8) (2024) 2308036.
- [42] L. Ding, M. Li, Y. Zhao, H. Zhang, J. Shang, J. Zhong, H. Sheng, C. Chen, J. Zhao, The vital role of surface Brønsted acid/base sites for the photocatalytic formation of free -OH radicals, *Appl. Catal. B: Environ.* 266 (2020) 118634.
- [43] X. Qin, P. Cao, X. Quan, K. Zhao, S. Chen, H. Yu, Y. Su, Highly efficient hydroxyl radicals production boosted by the atomically dispersed Fe and Co sites for

- heterogeneous electro-fenton oxidation, *Environ. Sci. Technol.* 57 (2023) 2907–2917.
- [44] X. Hu, J. Bao, D. Chen, S. Jalil Shah, S. Subhan, W. Gong, W. Li, X. Luan, Z. Zhao, Accelerating the Fe(III)/Fe(II) cycle via enhanced electronic effect in NH_2 -MIL-88B(Fe)/TPB-DMTP-COF composite for boosting photo-Fenton degradation of sulfamerazine, *J. Colloid Interface Sci.* 624 (2022) 121–136.
- [45] T. Skorjanc, D. Shetty, A. Trabolsi, Pollutant removal with organic macrocycle-based covalent organic polymers and frameworks, *Chem* 7 (2021) 882–918.